Varistor behavior in a ternary system based on SnO_2 doped with a hexavalent donor: SnO_2-MnO_2-WO_3

André Luís Weber Buonocore[a], Rodolpho Mouta[b*], Jherfson Castro Gomes[b], Clenilton Costa dos Santos[b], Eduardo Moraes Diniz[b], Manoel Carvalho Castro Junior[c], José Hilton Gomes Rangel[d], Ferdinando Marco Rodrigues Borges[e], Fábio Henrique Silva Sales[a], Marcelo Moizinho Oliveira[a]

[a] PPGEM, IFMA, Campus Monte Castelo, São Luís, MA, Brazil, 65030-005
[b] Departamento de Física, UFMA, Campus do Bacanga, São Luís, MA, Brazil, 65080-805
[c] Departamento de Ensino, IFMA, Campus Barreirinhas, Barreirinhas, MA, Brazil, 65590-000
[d] PPGQ, IFMA, Campus Monte Castelo, São Luís, MA, Brazil, 65030-005
[e] DMM, IFMA, Campus Monte Castelo, São Luís, MA, Brazil, 65030-005
[*]Corresponding author; E-mail: mouta.rodolpho@ufma.br.

Abstract

Pentavalent metals have been used as donors in tin dioxide, giving it varistor characteristics when associated with densifying agents as CoO or MnO_2. However, attempts to obtain varistor behavior in SnO_2-based ternary systems using hexavalent donors such as W^{6+} have been unsuccessful to date, leading to typical linear behavior. Here it is shown that one can achieve nonlinear behavior in this kind of system, given a suitable choice of densifying agent (MnO_2). In order to get insights into the role of WO_3 content on the potential barriers responsible for varistor properties, a combination of experimental and theoretical techniques was used. Measurements revealed two minor but relevant phases, Mn_3O_4, and $MnWO_4$, whose presence was explained by theoretical calculations and whose amount was estimated as a function of WO_3. This estimate revealed a correlation between Mn_3O_4 amount and varistor properties, interpreted with basis on Mn defects at SnO_2/Mn_3O_4 interfaces. WO_3 content was varied to optimize the varistor properties, resulting in nonlinear coefficient $\alpha \sim 6$, breakdown electric field $E_b > 10$ kV/cm and leakage current $I_l \sim 200\ \mu$A. This finding is expected to stimulate further investigations on SnO_2-based ternary systems containing hexavalent oxides, especially using other densifying agents, such as CoO.

Keywords: SnO_2; Varistor; Doping; Ceramic; Phase diagram; Raman spectroscopy

1 Introduction

Commercial varistors are composed mainly of zinc oxide (ZnO) with one or more dopants, whose main purpose is to improve nonlinear behavior.[1,2] TiO_2-, $SrTiO_3$-, and WO_3-based varistor systems have also been studied, [3–5] but none of them had the same or better performance than conventional ZnO-based systems. Simultaneous addition of dopants that increase the grain conductivity and help the formation of effective potential barriers at grain boundaries is a process widely used to obtain SnO_2-based varistors [6] with high nonlinear coefficients similar to ZnO used commercially. One approach to obtaining dense SnO_2-based ceramics with nonlinear characteristics is using small additions of pentavalent oxides such as Nb_2O_5,[7,8] along with bivalent oxides as sintering agents, such as CoO[9] and MnO_2[8].

One might expect similar behavior with the substitution of hexavalent oxides for pentavalent ones. However, to date, it has never been reported any ternary system presenting varistor behavior based only on SnO_2, an oxide responsible for densification and a hexavalent oxide. Perazolli *et al*. [10] analyzed the SnO_2–ZnO–WO_3 system, finding only a ceramic with insulating behavior, without nonlinear behavior characteristic of varistors. On the other hand, Margionte *et al*.[11] has reported a *quinary* system including additional CoO and Cr_2O_3 that reached a nonlinear coefficient (α) as high as 33. This finding indicates that the cause for the lack of varistor behavior may not be precisely WO_3, but rather its association with the densifying agent ZnO.

This paper shows, for the first time, that a SnO_2-based ternary system containing a hexavalent dopant can indeed exhibit varistor behavior (given a suitable densifying agent choice) similar to those containing pentavalent dopants. This possibility is demonstrated for the ternary system SnO_2–MnO_2–WO_3. The observed non-monotonic dependence of varistor properties with WO_3 content in this system was also explained, based on information gathered from an association of experimental and theoretical techniques.

2 Materials and methods

2.1 Experimental materials and methods

The oxide powders SMWx (x = 0, 5, 10, 15, 20, 25, 30) were prepared from SnO_2 (99.5%, Merck), MnO_2 (99.9%, Vetec) and WO_3 (99.9% Fluka), with molar ratios listed in Table 1. In order to obtain each product, the reagents were first mixed in an agate mortar using an agate pestle and then ball milled in isopropanol media in a Teflon jar with yttria-stabilized zirconia balls ($\phi = 5$ mm) for 24 h using a 5:1 balls:powder mass ratio at 30 rpm. After this, the mixed powder was dried at 70°C for 24 h, deagglomerated with an agate mortar, and sieved (100-mesh). Next, 0.2 g of powder was pressed into disc pellets by uniaxial cold pressing (60 MPa) using a $\phi = 9$ mm die and then sintered to 1300 °C for 2 h with a heating rate of 5 °C/min. After these 2 h, the furnace was turned off and let to cool down naturally to ambient temperature.

Table 1. Compositions of the SnO_2 – MnO_2 – WO_3 systems investigated.

System	Composition (mol%)		
	SnO_2	MnO_2	WO_3
SMW0	99.00	1.00	0.00
SMW5	98.95	1.00	0.05
SMW10	98.90	1.00	0.10
SMW15	98.85	1.00	0.15
SMW20	98.80	1.00	0.20
SMW25	98.75	1.00	0.25
SMW30	98.70	1.00	0.30

The resulting pellets were characterized at room temperature by X-ray diffraction (XRD), scanning electron microscopy (SEM), densitometry, energy dispersive spectroscopy (EDS), Raman spectroscopy and (I-V) tension-current DC measurements.

A Bruker D8 Discover diffractometer with CuKα radiation and a Lynxeye XE linear detector collected XRD data of pellets in the 2θ range of 10° – 70° with a step size of 0.02° (2θ) and counting time of 0.8s/step. The tube voltage and current were 40 kV and 40 mA, respectively.

Pellets morphologies were analyzed by SEM under high vacuum (FEI, model Quanta FEG 250, 1 to 30 kV) in BSE mode. The mean grain diameter was obtained according to ASTM E112-10 from the micrographs. Elemental mapping was performed by EDS (Ametek, model HX - 1001) with Apollo X - SDD detector. The apparent density of pellets was obtained *via* Archimedes method according to ASTM C-373-88.

Raman spectra were obtained using a Horiba-Jobin-Yvon triple spectrometer model T64000 equipped with a liquid N_2-cooled CCD, and 2 cm^{-1} spectrum resolution slit. Measurements employed a 532 nm green monochromatic laser beam emitted from a diode (LAS-532-100 HREV) operating at 14 mW.

Before DC electrical measurements, the opposite flat surfaces of each sintered pellet were sanded until the sample reached a thickness of ~0.7 mm, and then painted with silver paste, which was cured afterward. Tension-current (V-I) measurements were carried out under N_2 atmosphere with a Keithley high voltage supply, model 6517B, using the "staircase" function to sweep the voltage from 0 to 900 V in 20 V intervals with 0.2 seconds between measurements. Higher voltages were not used because currents higher than those measured could damage the equipment, according to the manufacturer instructions. Nonlinear coefficients were obtained by linear regression of points from 1 to 3.5 mA/cm^2, breakdown electric fields were taken at 1 mA/cm^2, and leakage currents were taken at 80% of the breakdown electric field.

2.2 Theoretical methods

Thermal stability of phases in the quaternary system Sn – Mn – W – O was investigated by constructing theoretical phase diagrams at finite temperatures. This system was regarded as isobaric, isothermal, open with respect to oxygen, and closed with respect to Sn, Mn, and W, which simulates the conditions during synthesis and measurements of the materials studied here.

The appropriate thermodynamic potential to describe the system's energetics in such conditions is the oxygen grand potential, defined as

$$\begin{aligned}\Phi\left(T,p,N_{Sn},N_{Mn},N_W,\mu_{O_2}\right)&\\ &= E\left(T,p,N_{Sn},N_{Mn},N_W,\mu_{O_2}\right)+pV\left(T,p,N_{Sn},N_{Mn},N_W,\mu_{O_2}\right)\\ &- TS\left(T,p,N_{Sn},N_{Mn},N_W,\mu_{O_2}\right)-\mu_{O_2}N_{O_2}\left(T,p,N_{Sn},N_{Mn},N_W,\mu_{O_2}\right)\\ &= G\left(T,p,N_{Sn},N_{Mn},N_W,\mu_{O_2}\right)-\mu_{O_2}N_{O_2}\left(T,p,N_{Sn},N_{Mn},N_W,\mu_{O_2}\right),\end{aligned} \quad (1)$$

where E, G, T, p, V, S and N_j are the internal energy, Gibbs energy, absolute temperature, pressure, volume, entropy and the number of atoms of species j of the phase, respectively.[12] μ_{O_2} is the oxygen chemical potential, which depends on temperature and oxygen partial pressure, p_{O_2}, according to the expression bellow:

$$\mu_{O_2}(T, p_{O_2}) = h_{O_2}(T) - Ts_{O_2}(T, p^0_{O_2}) + k_B T ln\left(\frac{p_{O_2}}{p^0_{O_2}}\right), \quad (2)$$

in which h_{O_2} and s_{O_2} are the enthalpy and the entropy of an oxygen molecule and $p^0_{O_2}$ is the reference pressure at which this entropy is evaluated.[12–15]

For each particular μ_{O_2}, p and T, one should calculate for all phases of the system the normalized oxygen grand potential, $\bar{\Phi}$, as a function of the fractions x_j of components j in Sn – Mn – W composition space,[12]

$$\bar{\Phi}(T, p, x_{Sn}, x_{Mn}, x_W, \mu_{O_2}) = \frac{\Phi(T, p, N_{Sn}, N_{Mn}, N_W, \mu_{O_2})}{N_{Sn} + N_{Mn} + N_W}, \quad (3)$$

then take the corresponding convex hull,[16] and construct a two-dimensional Sn – Mn – W Gibbs triangle with the projection of the stable nodes. However, for a condensed phase under pressures at the order of magnitude of atmospheric pressure or below, the term pV is negligible. Also, the entropy of oxygen gas is much larger than the entropy of condensed phases, so the term TS can be neglected compared to the term $TS_{O_2} = TN_{O_2}s_{O_2}$ that comes from the oxygen chemical potential. Thus, the Gibbs energy in Equation (1) can be approximated as the internal energy, which temperature dependence one may also disregard and adopt Density Functional Theory (DFT) calculations at 0 K values instead, once the term $\mu_{O_2}N_{O_2}$ carries the most significant effect of temperature change (the loss or absorption of oxygen). Such approximations are especially useful, once experimental temperature dependence of Gibbs energies are rarely available for all phases of a system and *ab initio* calculations for $T > 0$ usually require multiple phonon calculations for each phase.[17]

After simplifications above, the reduced oxygen grand potential becomes approximately

$$\bar{\Phi}(x_{Sn}, x_{Mn}, x_W, \mu_{O_2}) \approx \frac{E_{DFT}(0\ K) - \mu_{O_2}N_{O_2}}{N_{Sn} + N_{Mn} + N_W}, \quad (4)$$

where $x_j = N_j/(N_{Sn} + N_{Mn} + N_W)$ and the explicit dependence of the right-hand side quantities on state variables was dropped for brevity. This simpler expression was used to construct the oxygen grand potential phase diagrams of condensed phases as a function of the oxygen chemical potential, which now carries alone all temperature and oxygen partial pressure effects.

DFT energies[18] of the phases of the Sn – Mn – W – O system were collected from the Materials Project database[19,20] and used to construct the phase diagrams for a wide range of μ_{O_2} values *via* the Python Materials Genomics (pymatgen) code.[21] For further details on the overall methodology of the construction of phase diagrams from first principles, the reader is referred to references [12,15,22].

To convert the chemical potential ranges to explicit temperature ranges, one can isolate T in equation (2),

$$T = \frac{h_{O_2}(T) - \mu_{O_2}(T, p_{O_2})}{k_B ln\left(\frac{p_{O_2}}{p^0_{O_2}}\right) - s_{O_2}(T, p^0_{O_2})}, \quad (5)$$

and solve it iteratively: in the first cycle one evaluates the enthalpy and entropy of oxygen gas at room temperature, along with the input oxygen chemical potential, $\mu_{O_2}(T, p_{O_2})$, to estimate the corresponding temperature. In the next cycle, one revaluates the enthalpy and entropy at this new temperature and obtain a newer temperature estimate from them and from that same chemical potential provided as input. This procedure continues until temperature converges. The oxygen partial pressure used was $p_{O_2} = 0.21$ atm.

Since the phase diagrams constructed by the pymatgen code are actually for ranges of μ_O, we multiplied these values by a factor of two to obtain μ_{O_2} values and then substitute the latter at equation (5). Furthermore, to be consistent with the other energies taken from Materials Project and used to construct the phase diagrams, the energy of an oxygen molecule at 0 K as also taken from their database,[23] i.e.,

$$h_{O_2}(0\ K) = E_{O_2}(0\ K) = \mu_{O_2}(0\ K) = -9.871\ eV. \tag{6}$$

Thus, one can write the following expression for the oxygen enthalpy:

$$h_{O_2}(T) = \mu_{O_2}(0\ K) + \left(\Delta h_{O_2}\right)_{0\ K \to RT} + \left(\Delta h_{O_2}\right)_{RT \to T}(T). \tag{7}$$

The difference

$$\left(\Delta h_{O_2}\right)_{0\ K \to RT} \equiv h_{O_2}(298.15\ K) - h_{O_2}(0\ K) = 8.999 \times 10^{-2}\ eV \tag{8}$$

was obtained from the JANAF thermochemical tables,[24] whereas the difference

$$\left(\Delta h_{O_2}\right)_{RT \to T}(T) \equiv h_{O_2}(T) - h_{O_2}(298.15\ K) \tag{9}$$

was obtained from fits of thermochemical data of oxygen gas from the same table to Shomate equation in the range 100 K – 6000 K,[25] and is given by the expression that follows:[13,25]

$$\left(\Delta h_{O_2}\right)_{RT \to T}(T) = 1000\left[A\left(\frac{T}{1000}\right) + \frac{B}{2}\left(\frac{T}{1000}\right)^2 + \frac{C}{3}\left(\frac{T}{1000}\right)^3 + \frac{D}{4}\left(\frac{T}{1000}\right)^4 - E\left(\frac{1000}{T}\right) + F\right]. \tag{10}$$

Thus, equation (5) becomes

$$T = \frac{-9.781\ eV + \left(\Delta h_{O_2}\right)_{RT \to T}(T) - 2\mu_O(T, p_{O_2})}{k_B ln\left(\frac{p_{O_2}}{p^0_{O_2}}\right) - s_{O_2}(T, p^0_{O_2})}. \tag{11}$$

The entropy values at a reference pressure of $p^0_{O_2} = 0.1$ MPa were also obtained from the same fits to Shomate equation, and are given by the expression bellow:[13,25]

$$s_{O_2}(T) = Aln\left(\frac{T}{1000}\right) + B\left(\frac{T}{1000}\right) + \frac{C}{2}\left(\frac{T}{1000}\right)^2 + \frac{D}{3}\left(\frac{T}{1000}\right)^3 - \frac{E}{2}\left(\frac{1000}{T}\right)^2 + G. \tag{12}$$

The Shomate equation coefficients used here are shown in Table 2.

Table 2. Shomate equation coefficients from JANAF thermochemical tables at three temperature ranges.[13,25]

Coefficient	$100\ K - 700\ K$	$700\ K - 2000\ K$	$2000\ K - 6000\ K$
$A\ (J/mol \cdot K)$	31.32234	30.03235	20.91111
$B\ (J/mol \cdot K^2)$	−20.23531	8.772972	10.72071
$C\ (J/mol \cdot K^3)$	57.86644	−3.988133	−2.020498
$D\ (J/mol \cdot K^4)$	−36.50624	0.788313	0.146449
$E\ (JK/mol)$	−0.007374	−0.741599	9.245722
$F\ (J/mol)$	−8.903471	−11.32468	5.337651
$G\ (J/mol \cdot K)$	246.7945	236.1663	237.6185

3 Results and Discussion

3.1 X-ray diffraction

In order to identify the phases present after sintering, XRD measurements were performed on the pellets, and the diffractograms obtained are shown in Figure 1. Diffractograms of SMW0, SMW5 and SMW10 showed only the cassiterite (SnO_2, tetragonal, space group #136) phase, similar to that observed by Margionte *et al.* [26]. From compositions SMW15 to SMW30, XRD also detected a small amount of a secondary phase, identified as hübnerite ($MnWO_4$, monoclinic, space group #13). The presence of this secondary phase from pellet SMW15 onwards indicates that W solubility on SnO_2 is lower than 0,10% in mol. Interestingly, the observed relative intensities of this phase differ significantly from the reference powder pattern, indicating that the crystallites of this phase have strong preferential orientation: some crystallographic planes will be preferably parallel to the pellet's surface and result in higher intensity peaks, while planes perpendicular to the surface will have their intensity significantly lowered.

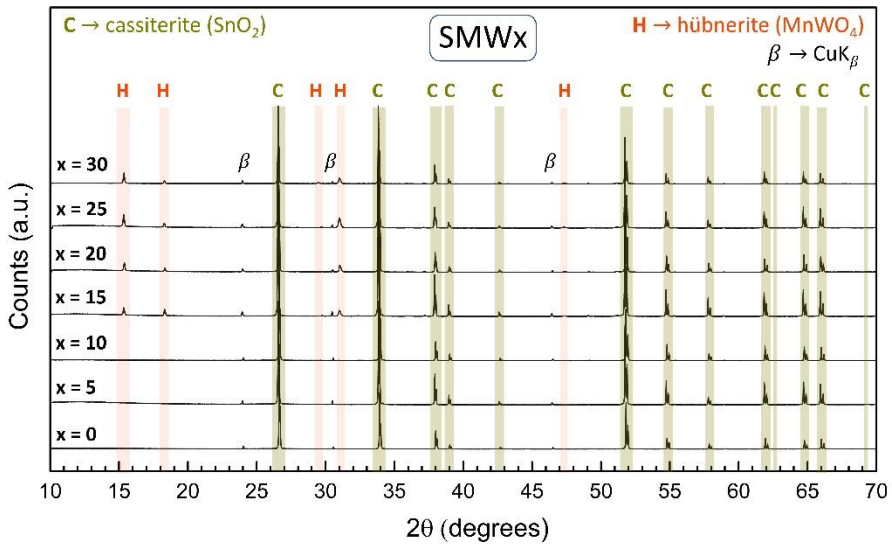

Figure 1. Diffractograms of sintered pellets SMWx (x = 0, 5, 10, 15, 20, 25, 30). All peaks belonging to the SnO_2 pattern in this 2θ range were highlighted and assigned, as well as the most intense observed peaks of $MnWO_4$. Small peaks assigned as β are due to CuK_β radiation and are associated to the three more intense SnO_2 peaks.

3.2 Scanning electron microscopy (SEM), energy dispersive spectroscopy (EDS), and densitometry

Since the interplay between grains, grain boundaries and precipitates have a significant impact on the properties of a varistor material, the microstructure of SMWx pellets was investigated by SEM, and the obtained micrographs are shown in Figure 2.

The microstructure of SMW0 comprises grains of a predominant phase (lighter shades of grey in Figure 2) and a sparse precipitate phase at triple points (dark grey in Figure 2). Addition of WO_3 up to 0.10% in mol promoted a significant increase of the precipitate phase, as seen in SMW5 and SMW10 micrographs. However, the amount of this precipitate phase progressively decreases at higher WO_3 concentrations ($\geq$ 0.15% in mol), accompanied by the increase of yet another precipitate phase (light grey needles/plates in Figure 2), whose onset traces back to the SMW10 micrograph. Interestingly, the two precipitates seem to be competing phases, once a local abundance of one accompanies a shortage of the other.

Another feature observed is the presence of pores at higher concentrations of WO_3, especially at SMW20 and SMW25 micrographs. This porosity, along with the increase of precipitate phases, resulted in a nearly monotonic reduction of relative density from 97.6% (SMW0) to 91.3% (SMW30), as shown in Table 3. The mean grain size, on the other hand, increased with the first WO_3 addition but remained approximately constant with higher WO_3 contents.

Since the main phase detected by XRD was SnO_2, and the $MnWO_4$ phase only was detected from composition SMW15 onwards, one can safely assign grains as SnO_2 and the needle-like/plate-like precipitates as $MnWO_4$. The morphology of this latter precipitate is also compatible with the preferential orientation of $MnWO_4$ indicated by XRD. However, the identity of the other precipitate phase, at triple points, could not be deduced by the diffractograms and micrographs alone. In order to help elucidate this point and provide insights regarding the solubility of Mn and W on SnO_2, EDS measurements were also performed on some of the pellets.

According to the EDS mapping of SMW10 (Figure 3), the precipitate phase at triple points is composed mainly of Mn and O, indicating it is a manganese oxide. EDS of this precipitate at SMW15 also supports this interpretation, as seen at “spot 4” in Figure 4. Also, even at some triple points without noticeable precipitates in the micrograph of SMW15, as at “spot 2” in Figure 4, EDS showed a high concentration of Mn. Therefore, it appears that Mn has a strong preference for triple points among SnO_2 grains, and this may have led to nucleation and growth of manganese oxide precipitates at these locations.

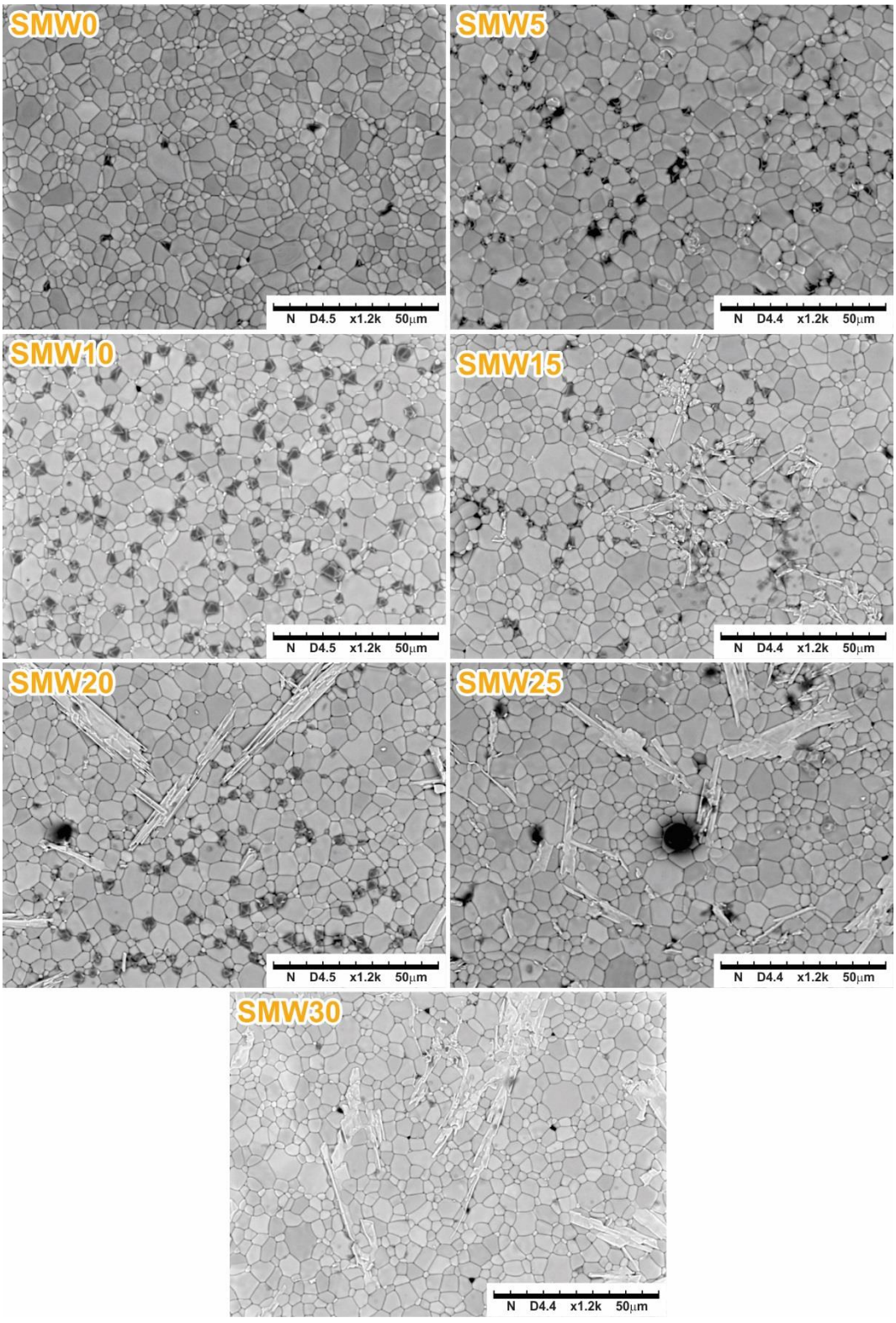

Figure 2. SEM Micrographs of SMWx (x = 0, 5, 10, 15, 20, 25, 30) pellets. The length of the bar at the right bottom of each image is 50 μm.

Table 3. Mean grain size and relative density for studied systems.

System	Mean Grain Size (μm)	Relative Density (%)
SMW0	5.9 ± 0.1	97.6 ± 0.9
SMW5	7.0 ± 0.2	96.7 ± 0.7
SMW10	7.0 ± 0.2	96.5 ± 1.0
SMW15	7.2 ± 0.1	95.9 ± 0.5
SMW20	7.3 ± 0.1	93.3 ± 1.1
SMW25	7.3 ± 0.2	91.2 ± 1.2
SMW30	7.2 ± 0.1	91.3 ± 1.4

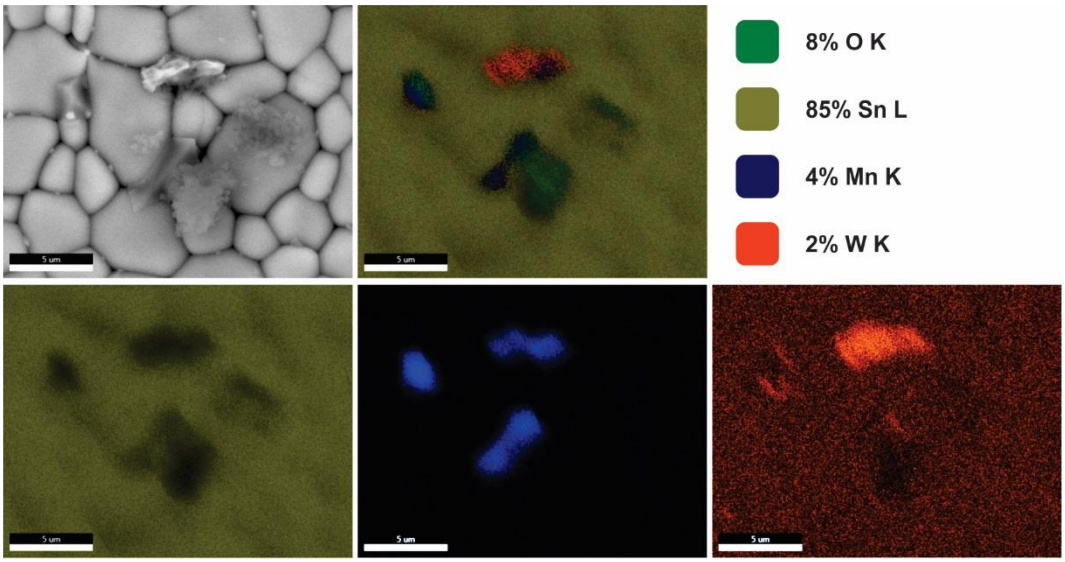

Figure 3. EDS Mapping for SMW10 system. The length of the bar at the left bottom of each image is 5 μm.

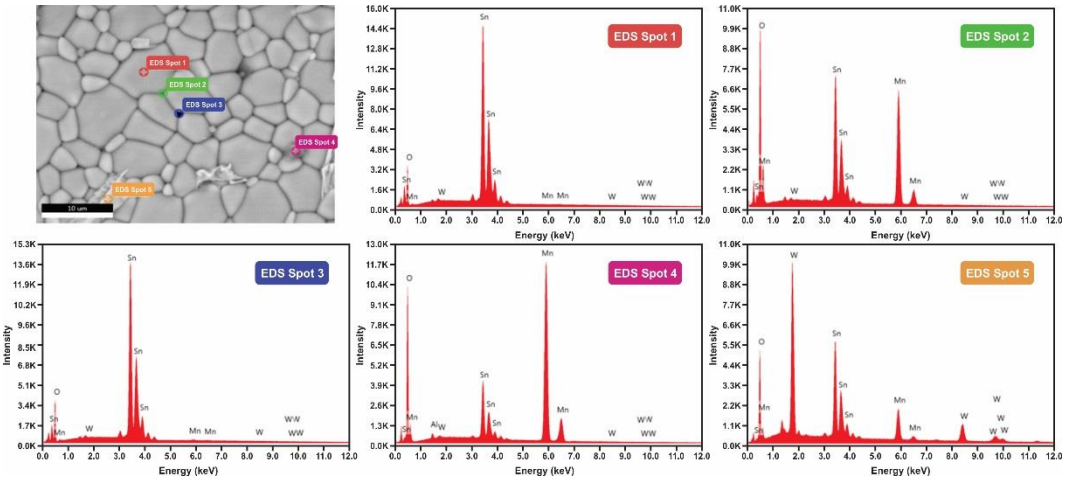

Figure 4. SEM/EDS for SMW15 system. The length of the bar at the left bottom of the micrograph is 10 μm.

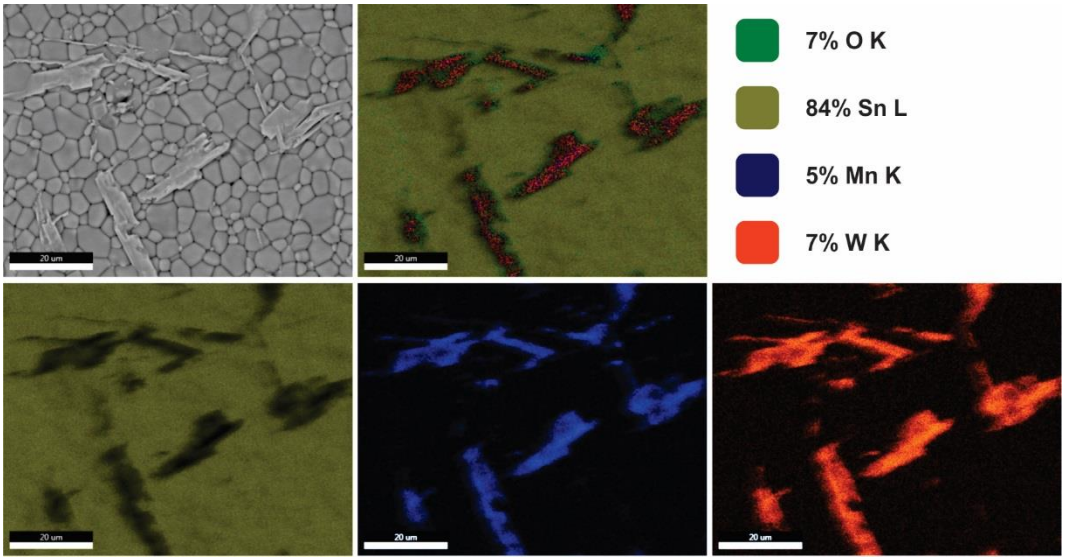

Figure 5. EDS Mapping for SMW25 system. The length of the bar at the left bottom of each image is 20 μm.

As for the grains, they are indeed composed mainly of Sn and O, according to EDS mappings of SMW10 and SMW25 (Figure 3 and Figure 5, respectively) and EDS at "spot 1" of SMW15 (Figure 4). However, they also contain a noticeable amount of W, as evident from EDS mappings of SMW10 and SMW25 and the low (but not negligible) intensity peak at 1.775 keV corresponding to W atoms at "spot 1" of SMW15 (Figure 3, Figure 5 and Figure 4, respectively). On the other hand, Mn could not be detected inside grains of SMW10 and SMW15 (Figure 3 and Figure 4), although its presence is evident in the case of SMW25 (Figure 5). This low solubility of Mn in SnO_2 has also been reported by Gouvea *et al.* [27,28] and may be responsible for the Mn preference for grain boundaries shown above. Besides, the even distribution of W in the grains seems to decrease manganese solubility even further, raising the manganese oxide precipitate concentration at boundary region. Orlandi *et al.* observed similar behavior.[8]

The needle-like/plate-like precipitates were confirmed to be an Mn- and W-rich, Sn-poor phase (Figure 3 and Figure 5), supporting its assignment as the $MnWO_4$ phase identified by DRX. As discussed above, this phase forms at the expense of manganese. This manganese decrease explains the trends of mean grain size and relative density observed in Table 3, as Gouvea *et al.* have shown that the presence of manganese cations on grain surface controls grain growth and densification of SnO_2.[27] Therefore, $MnWO_4$ formation hindered the densification mechanism and favored grain growth mechanism.

3.3 Raman spectroscopy

Raman spectroscopy was then used to identify whether the precipitates at triple points were indeed a manganese oxide and, if so, which one. Grains, grain boundaries at triple points, and the needle-like/plate-like precipitates were also probed to endorse the previous conclusions draw

from DRX, SEM, and EDS. Phases were identified by comparing the measured spectra with those on the RRUFF Project database.[29]

As shown in Figure 6, the Raman spectra of the manganese oxide precipitate (spot 1 in the figure) of SMW10 and SMW20 match that of Mn_3O_4 (tetragonal, space group #141; RRUFF ID #R040090), whose most intense vibrational modes are those at 315, 369 and 657 cm^{-1}. They correspond to the out-of-plane bending modes of Mn_3O_4, the asymmetric stretch of bridge oxygen species (Mn-O-Mn), and the symmetric stretch of Mn_3O_4 groups, respectively. [30–32]

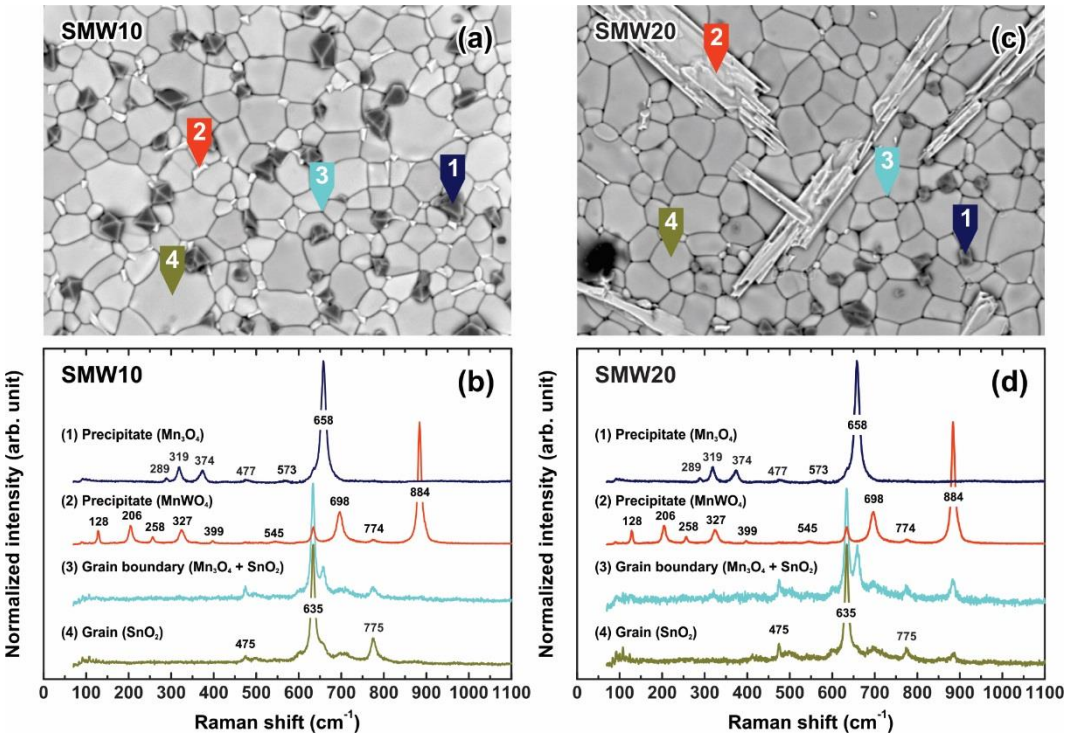

Figure 6. Raman spectra recorded at the grain, grain boundary and precipitates positions in the (b) SMW10 and (d) SMW20 samples, as shown in their respective SEM micrographs (a) and (c).

Raman spectroscopy also confirmed that grains of SMW10 and SMW20 are basically composed of SnO_2 (RRUFF ID #R060563), since their Raman spectra (spot 4 in Figure 6) show mainly the cassiterite vibrational modes: the three most intense bands located at 474 cm^{-1}, 634 cm^{-1} and 774 cm^{-1} associated to E_g, A_{1g} and B_{2g} vibrational modes, respectively.

Grain boundaries at triple points of SMW10 and SMW20 are composed by both SnO_2 and Mn_3O_4 (spot 3 in Figure 6), which explains the high concentration of Mn found by EDS in these regions.

The assignment of needle-like/plate-like precipitates as $MnWO_4$ (RRUFF ID #R050139) was also endorsed by their Raman spectra (spot 2 in Figure 6) since the measured frequencies of the main vibrational modes of these precipitates are identical to those from literature (Table 4).

Table 4. Raman spectroscopy vibrational modes of the needle-like/plate-like precipitate, compared to the vibrational modes and their respective atomic movements found in the literature for $MnWO_4$.

Mode	Raman frequencies (cm^{-1})		Atomic movements
	This work	Ref. [33]	
A_g	128-129	129	Mn(y) W(y)
A_g	206-208	206	W(y) Mn(y)
A_g	257-258	258	O2(xyz) W(y) Mn(y)
A_g	326-327	327	O2(yz) O1(xyz) Mn(y)
A_g	397-398	397	O2(xy) O1(xz) W(y)
A_g	545-546	545	O1(yz) O2(xyz) Mn(y) W(y)
A_g	697-698	698	O1(xz) W(y)
A_g	884	885	O2(xyz) W(y)
B_g	774-776	774	O2(xyz) W(xz)

3.4 Distribution of Mn and W over grains, precipitates and grain boundaries

Next, based on information gathered from XDR, SEM, EDS, and Raman spectroscopy, it is presented estimates of SnO_2:Mn_3O_4:$MnWO_4$ molar ratio, Mn_3O_4 distribution over grain boundaries and precipitates, Mn and W solubility in SnO_2 grains, and amount of oxygen released during sintering. Most of these quantities vary with W content and, as demonstrated below, their interplay results in the behavior observed as x increased: increase of Mn_3O_4 precipitates when W is first introduced, and then the appearance and increase of $MnWO_4$ precipitates accompanied by a decrease of Mn_3O_4 precipitates. Also, as shown later, the dependence of the amount of overall Mn_3O_4 phases on x is strongly connected to the varistor properties of SMWx systems, so it is important to estimate this dependence, which could not be directly obtained by experiments.

One can state the overall reaction in the SMWx systems as

$$\begin{aligned}(0.99-x)SnO_2 + xWO_3 + 0.01MnO_2 \\ \longrightarrow \alpha Sn_{1-y-(3z/2)}Mn_yW_zO_{2-(y/2)} + \beta MnWO_4 + \gamma_p(Mn_3O_4)_p \\ + \gamma_{gb}(Mn_3O_4)_{gb} + \delta O_2\uparrow,\end{aligned} \tag{13}$$

where x is the molar fraction of WO_3 reactant ($= x/10^4$), y and z are the concentration of Mn and W dopants in SnO_2, respectively, and subscripts p and gb refer to Mn_3O_4 precipitates and Mn_3O_4 in grain boundaries, respectively. It was assumed that the oxidation state of Mn inside SnO_2 grains is 3+, although a different value such as 2+ or 4+ would only change the amount of oxygen released and of oxygen vacancies, without implications for the secondary phases. γ_p and γ_{gb} can be condensed in a single coefficient,

$$\gamma = \gamma_p + \gamma_{gb}\,, \tag{14}$$

corresponding to Mn_3O_4 phases in general, irrespective of where they are located in the pellets.

Below, α, β, γ_p, γ_{gb}, γ, δ, y and z are calculated as a function of x based on two assumptions. One is that Mn and W have nearly equal solubility in SnO_2 but compete with each other, with the latter being more favorable than the former. This is, Mn amount in SnO_2 is maximum when there

is no addition of W and decreases as W is added, until Mn becomes eventually absent in SnO_2 at some critical $x = x_{c1}$, at which W concentration in SnO_2 reaches its solubility limit, z_{max}:

$$y + z = cte = z_{max} \, . \tag{15}$$

Within the W solubility limit, all W atoms are found as dopants in SnO_2, whereas beyond that limit the remainder of W atoms begins to form a $MnWO_4$ precipitate. The other assumption is that Mn_3O_4 is located preferably at grain boundaries up to a molar limit $\gamma_{gb,max}$. Since the amount of overall Mn_3O_4 exceeds this limit for lower values of x, the amount at grain boundaries is essentially insensitive to x (and equals to $\gamma_{gb,max}$) until some critical $x = x_{c2}$, at which all Mn_3O_4 precipitates have been consumed to form $MnWO_4$. From this point onwards it is the Mn_3O_4 at grain boundaries that is consumed:

$$\gamma_{gb} = \begin{cases} \gamma_{gb,max} & x < x_{c2} \\ \gamma & x \geq x_{c2} \end{cases} \, ; \tag{16}$$

$$\gamma_p = \begin{cases} \gamma - \gamma_{gb,max} & x < x_{c2} \\ 0 & x \geq x_{c2} \end{cases} \, . \tag{17}$$

Although measurements performed here could not directly access these two assumptions, it is evident that their consequences, as discussed above, are in complete agreement with SEM and EDS results.

Balancing of chemical equation (13) leads to the following coefficients α, β, γ and δ:

$$\alpha = \frac{2(0.99 - x)}{2(1 - z_{max}) - z} \, ; \tag{18}$$

$$\beta = x - \alpha z \, ; \tag{19}$$

$$\gamma = \frac{0.01 - \alpha(z_{max} - z) - \beta}{3} \, ; \tag{20}$$

$$\delta = \frac{2(2 + x) - (4 + z - z_{max})\alpha - 8(\beta + \gamma)}{4} \, . \tag{21}$$

Equation (15) was used to eliminate y. From equations (18) and (19), and bearing in mind that $\beta = 0$ for $x < x_{c1}$, one can calculate the fraction z of W atoms at Sn sites in SnO_2 as

$$z = \begin{cases} \dfrac{2x(1 - z_{max})}{1.98 - x} & (x < x_{c1}) \\ z_{max} & (x \geq x_{c1}) \end{cases} \, . \tag{22}$$

The values of z_{max} and $\gamma_{gb,max}$ were obtained by demanding that z is continuous at x_{c1} and that γ_{gb} is continuous at x_{c2}, respectively. This results:

$$z_{max} = \frac{2x_{c1}}{1.98 + x_{c1}} \, ; \tag{23}$$

$$\gamma_{gb,max} = \frac{0.02 + 1.95z_{max} + x_{c2}(z_{max} - 2)}{3(2 - 3z_{max})} \, . \tag{24}$$

Thus, one may estimate x_{c1} and x_{c2} from SEM measurements, obtain z_{max} and $\gamma_{gb,max}$ from equations (23) and (24), obtain z from Equation (22), and then calculate α, β, γ, γ_{gb}, γ_p and δ from equations (18), (19), (20), (16), (17) and (21), respectively. Since traces of $MnWO_4$ phase start to appear in micrographs at $x = 0.10\%$, the onset of its formation (x_{c1}) lies somewhere in between $x = 0.05\%$ and $x = 0.10\%$. Also, since the absence of Mn_3O_4 precipitates are first

noted at $x = 0.25\%$, the onset of their depletion occurs at some point in between $x = 0.20\%$ and $x = 0.25\%$. Thus, x_{c1} and x_{c2} were estimated as the midpoints of these ranges, i.e.,

$$x_{c1} = 0.075\%\,; \tag{25}$$
$$x_{c2} = 0.225\%\ , \tag{26}$$

although the actual values may differ slightly from these adopted here. Such values lead

$$z_{max} = 0.076\%\ ; \tag{27}$$
$$\gamma_{gb,max} = 0.283\%\ . \tag{28}$$

The values of all estimated quantities for each SMWx system are presented in Table 5. It is evident that coefficients of Mn_3O_4 precipitates and $MnWO_4$ follow the qualitative trend observed in SEM micrographs and discussed at the beginning of this section. The behavior of the coefficient of overall Mn_3O_4 phases, on the other hand, could not be directly inferred from experiments and is calculated as slightly different from that of Mn_3O_4 precipitates. Both initially increase with x, reach a peak at x_{c1}, and then eventually decrease to values lower than that of $x = 0$. But the former assumed a non-null value at greater x values. Interestingly, this is essentially the same trend seen in most varistor properties of the SMWx systems, as shown later.

Table 5. Dependence of terms in Equation (13) on W content, separated by range. In the first range, all W atoms are inside SnO_2, so $MnWO_4$ is not present yet. In the second, W atoms reach their solubility limit in SnO_2 and their excess form a $MnWO_4$ phase at the expense of Mn_3O_4 precipitates. In the third range, Mn_3O_4 precipitates are no longer present, and part of the $MnWO_4$ phase now is formed at the expense of Mn_3O_4 at grain boundaries.

x (%)	Range	z (%)	α (%)	β (%)	γ (%)	γ_{gb} (%)	γ_p (%)	δ (%)
0.00	$x < x_{c1}$	0.000	99.075	0.000	0.308	0.283	0.025	0.327
0.05		0.050	99.050	0.000	0.325	0.283	0.042	0.331
0.10	$x_{c1} \le x < x_{c2}$	0.076	99.012	0.025	0.325	0.283	0.042	0.338
0.15		0.076	98.962	0.075	0.308	0.283	0.025	0.346
0.20		0.076	98.912	0.125	0.292	0.283	0.008	0.354
0.25	$x \ge x_{c2}$	0.076	98.862	0.175	0.275	0.275	0.000	0.363
0.30		0.076	98.812	0.225	0.258	0.258	0.000	0.371

3.5 Thermodynamic stability from first principles

Whereas the presence of secondary phases in the pellets may be explained by a low solubility of Mn and W in SnO_2 as discussed in the previous section, it was less obvious why measurements identified specifically the phases $MnWO_4$ and Mn_3O_4, instead of starting oxides WO_3 and MnO_2.

To shed light on this, the relative thermodynamic stability of these and remaining phases in the system Sn-Mn-W-O was investigated by constructing the theoretical oxygen grand potential phase diagrams shown in Figure 7(a)-(d). Each one displays the thermodynamically stable phases (colored nodes) at a specific temperature range. For any composition not located precisely at a node, a mixture of two or three phases will occur, depending on whether this composition lies at a line connecting two nodes or inside a triangle formed by three nodes. In the first case, the stable phases at that composition are those at the two nearest nodes in that line, whereas in the latter case are those at the triangle vertices nodes.[12]

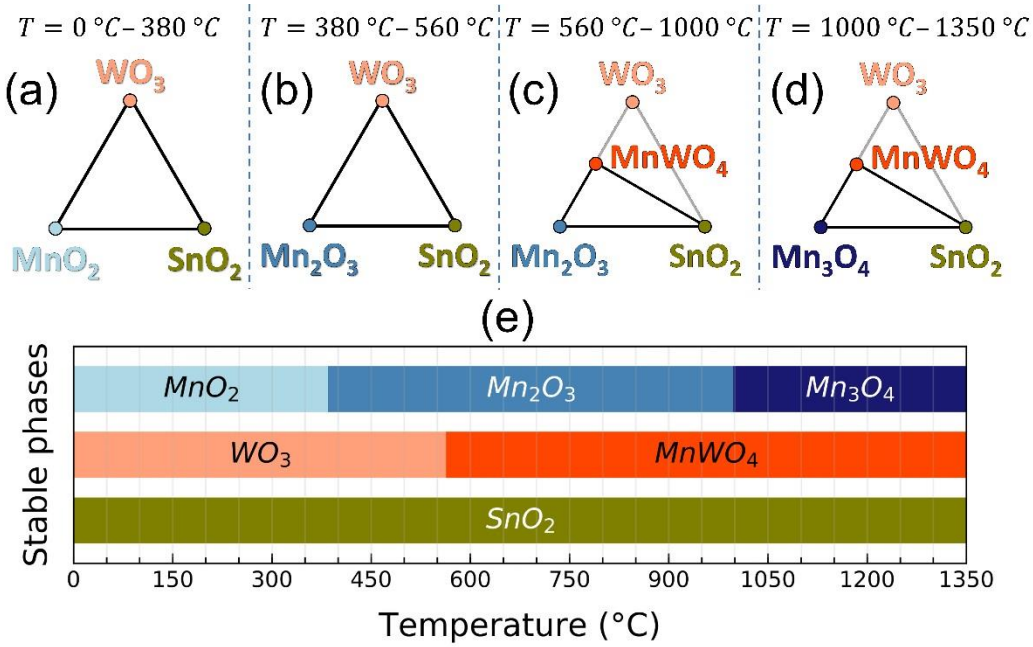

Figure 7. (a)-(d) Oxygen grand potential phase diagrams from first principles for four temperature ranges. (e) The three thermodynamically stable phases (nodes of the black edges triangles inside of which are the compositions investigated here) as a function of temperature.

Owing to the small fraction of Mn and W in the pellets, all compositions synthesized are located very close to the Sn corner (bottom right vertex) at the phase diagram, lying inside a triangle (the one with black edges in Figure 7(a)-(d)) formed by the only three expected stable phases for this range of compositions.

Figure 7(e) shows the evolution of these phases along the heating process. SnO_2 is thermodynamically stable throughout the whole temperature range investigated (0 – 1350 °C). MnO_2, on the other hand, is predicted to decompose to Mn_2O_3 at ~380 °C, which in turn decomposes to Mn_3O_4 at ~1000 °C. Then Mn_3O_4 remains stable at least until 1350 °C. At the Sn:Mn:W compositions considered here, WO_3 is stable until ~560 °C. At this temperature, it reacts with part of the Mn_2O_3 to form $MnWO_4$, which is still stable at 1350 °C.

After cooling down to room temperature, the thermodynamically stable phases are SnO_2, MnO_2 and WO_3 again. However, a not high enough atomic mobility at the transition temperatures [22] or a high cooling rate, or a combination of both, can kinetically stabilize $MnWO_4$ and Mn_3O_4, because they would reach room temperature before significant diffusion occurs, preventing the decomposition of these phases. As mentioned in Section 2.1, the furnace was shut down immediately after it spent the 2h at 1350 °C. Therefore, as the cooling rate was the highest possible without opening the furnace and quenching the pellets, it is not surprising that $MnWO_4$ and Mn_3O_4 were the precipitates identified by measurements, instead of starting oxides WO_3 and MnO_2.

Literature data support both the successive formation of Mn_2O_3, Mn_3O_4, and $MnWO_4$ during heating and the kinetic stabilization of the two latter at room temperature. For instance, after $MnWO_4$ is synthesized at high temperatures from manganese and tungsten sources, it remains stable at room temperature instead of decomposing to MnO_2 and WO_3.[34] Similar behavior is observed to Mn_3O_4, that can be obtained by heating MnO_2 at 1000 – 1050 °C in air and then cooling it down to room temperature.[35,36]

The effect of oxygen partial pressure, p_{O_2}, on the predicted reduction reactions was also investigated and is shown in the modified Ellingham diagram of Figure 8. Labels correspond to reactions listed in Table 6. The intercept of each reaction line with the temperature axis gives the temperature at which the reaction becomes thermodynamically favorable at $p_{O_2} = 1$ atm. At lower pressures, the reduction temperature is that at which the reaction line intercepts the corresponding pressure line.[12]

According to our predictions, using an oxygen-rich atmosphere ($p_{O_2} > 0.21$ atm) instead of air ($p_{O_2} = 0.21$ atm) has little effect on reduction temperatures, increasing them by only ~50 °C or less. An oxygen-poor atmosphere (inert gas or vacuum), on the other hand, can decrease reduction temperatures by hundreds of degrees, depending on how low the oxygen partial pressure is. However, in both cases, the conclusions drawn above stand the same, because at high temperatures the phases are still SnO_2, Mn_3O_4 and, $MnWO_4$, which are kinetically stabilized at room temperature by the high cooling rate.

Aside from the three reactions deduced *via* phase diagrams, two other reactions were considered, involving the formation of $MnWO_4$ from MnO_2 or Mn3O4, instead of Mn_2O_3 (reactions 1 and 3 in Table 6). $MnWO_4$ formation from Mn_3O_4 is favored already at low temperatures, but this only can happen if Mn_3O_4 is present, so $MnWO_4$ formation is delayed until the system reaches high temperatures. However, by this point, MnWO4 has already been formed from Mn_2O_3. $MnWO_4$ formation from MnO_2 is favored ~100 °C before from Mn_2O_3, so it may take place if MnO_2 has not been wholly reduced to Mn_2O_3 yet at this temperature due to kinetic reasons.

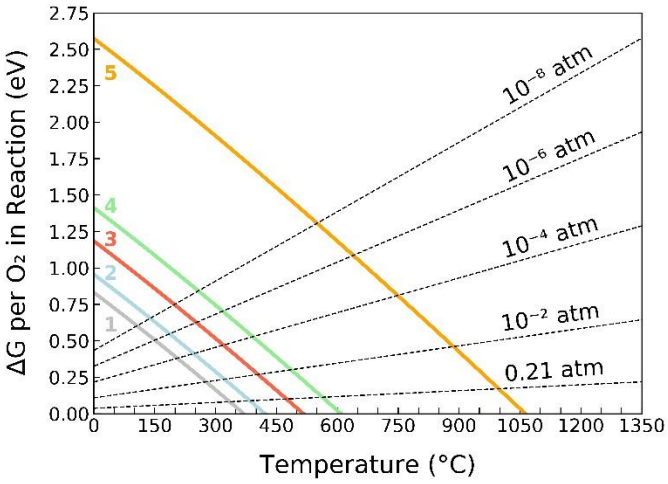

Figure 8. Modified Ellingham diagram for equations in Table 6. Lines with negative slope indicate oxygen partial pressure. Each reduction temperature is read from the intercept of the

reaction line with the temperature axis (at oxygen partial pressure of 1 atm), or with the appropriate pressure line (at an oxygen partial pressure lower than 1 atm).

Table 6. Reactions considered in Figure 8 and the labels used.

Label	Reaction
1	$2Mn_3O_4 + 6WO_3 \rightarrow 6MnWO_4 + O_2$
2	$4MnO_2 \rightarrow 2Mn_2O_3 + O_2$
3	$2MnO_2 + 2WO_3 \rightarrow 2MnWO_4 + O_2$
4	$2Mn_2O_3 + 4WO_3 \rightarrow 4MnWO_4 + O_2$
5	$6Mn_2O_3 \rightarrow 4Mn_3O_4 + O_2$

3.6 DC Tension-current (V-I) measurements

In a varistor, high nonlinear coefficient (α) and breakdown electric field (E_b), as well as low leakage current (I_l), are desirable for commercial application. As shown by the expression

$$j = KE^{\alpha}\,, \tag{29}$$

α is a measure of the nonlinearity: the greater this parameter is, the better the varistor; $\alpha = 1$, on the other hand, corresponds to ordinary linear behavior. E_b specifies the maximum operation voltage of the varistor and is proportional to the number of effective potential barriers (which decrease with increasing grain size) in grain boundary regions and also to their height. I_l is the current due to electrons that tunnel these barriers or that pass through grain boundaries where an effective barrier is absent; thus, a low leakage current is indicative of barriers effectiveness.

In order to evaluate the impact of WO_3 addition on these varistor properties of MnO_2-doped SnO_2, E *vs.* j curves were first obtained (Figure 9), from which α, E_b and I_l were derived (Figure 10).

Among the SMWx systems, SMW5 and SMW10 presented the highest nonlinear coefficient, 6.1. This α value is similar (although a little lower) to those of CoO- or MnO_2-doped SnO_2 systems with the addition of Nb_2O_5,[8] where pentavalent Nb acted as a dopant in SnO_2 (Table 7). More importantly, this α value of 6.1 demonstrates that WO_3 addition is a viable strategy for increasing α, given a suitable choice of densifying agent. Such choice appears to be crucial: while MnO_2, used here, led to increased α, ZnO actually leads to linear behavior (Table 7).[10,26] It is possible that a densifying agent other than ZnO and MnO_2 could result in even higher α values, which warrants further investigation.

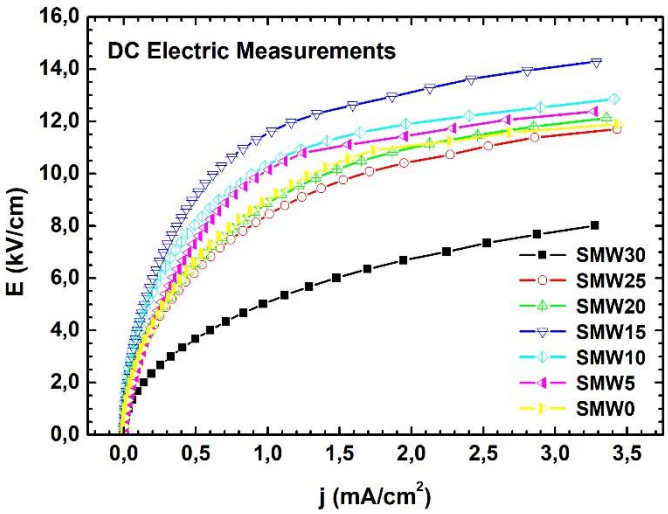

Figure 9. Electric field *vs.* current density curves. Voltage was swept in the range 0-900 V with a 20 V step and 0.2 s between steps. α was obtained by fitting Equation (29) in the range 1-3.5 mA/cm^2, E_b was taken at 1 mA/cm^2 and I_l was taken at 80% of the breakdown electric field.

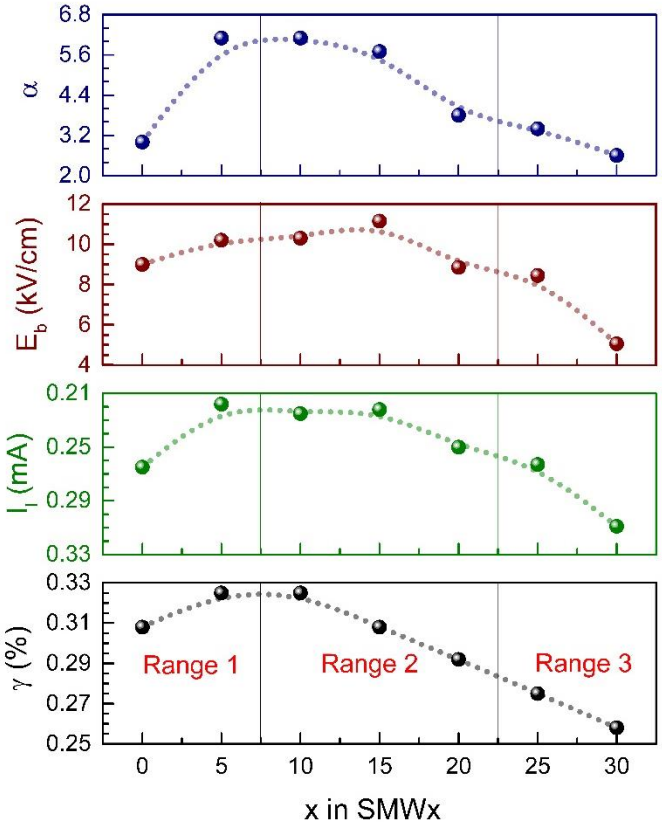

Figure 10. Nonlinear coefficient (α), breakdown electric field (E_b) and leakage current (I_l) for SMWx systems, obtained from curves in Figure 9. Dotted lines are guides to the eye. The coefficient of overall Mn_3O_4 phases (γ) in Equation (13), which is proportional to the relative

amount of Mn_3O_4 present in grain boundaries and as precipitates, is also shown for comparison. The three ranges are those discussed in Section 3.4.

SMW15 had the highest E_b of 11.15 kV/cm, although all three SMWx systems in the range x = 5 – 15 had E_b values above 10 kV/cm, which is greater than those of ternary CoO- or MnO_2-doped SnO_2 systems with the addition of Nb_2O_5.

SMW5 presented the lowest leakage current of 218 μA among SMWx systems. Such value is still high in comparison with commercial SnO_2-based varistors, which have I_l~50 μA. This indicates the existence of non-effective barriers at the grain boundary region.[8]

Table 7. SMW10 nonlinear coefficient and breakdown electric field compared to those of ternary systems in literature at their respective optimal compositions.

Reference	System	α	E_b (kV/cm)
This work (SMW10)	SnO_2-MnO_2-WO_3	6.1	10.3
Pianaro *et al.* [7]	SnO_2-CoO-Nb_2O_5	8	1.87
Orlandi *et al.* [8]	SnO_2-MnO_2-Nb_2O_5	7.3	9.35
Perazolli *et al.* [10]	SnO_2-ZnO-WO_3	~1 *	N/A *

* This system did not present nonlinear behavior.

It is evident in Figure 10 a correlation between the amount of Mn_3O_4 in the system and the varistor properties, especially α and I_l. This correlation holds even if a higher (but ≤ 0.10%) or slightly lower value for x_{c1} is adopted, since this would essentially only shift the γ peak position to this new (but very close) value. Adoption of a different x_{c2} would also not be a concern, since γ is independent of this parameter.

Such correlation was expected since Mn atoms act as donor metals, [37] segregating and thus promoting an increase of potential barrier at SnO_2/Mn_3O_4 interfaces by insertion of defects at the outermost atomic layers of SnO_2 according to the following reaction (in Kröger-Vink notation):

$$Mn_3O_4 \xrightarrow{SnO_2} Mn''_{Sn} + 2Mn'_{Sn} + 2V_O^{\circ\circ} + 4O_O^{\times} \ . \quad (30)$$

The presence of these negatively-charged defects favors adsorption of different oxygen species, aiding potential barrier formation and improving varistor properties of systems. [38,39] Thus, the higher the amount of Mn_3O_4 in the system, the better the varistor properties, as observed in Figure 10.

4 Conclusions

The SnO_2-MnO_2-WO_3 varistor system is a phase mixture for all compositions investigated. The identity of these phases and their location were identified using a combination of SEM, EDS, XRD and Raman measurements, as follow. The system without WO_3 (SMW0) exhibited SnO_2 grains, Mn_3O_4 precipitates and probably Mn_3O_4 also at grain boundaries since this latter phase was found at grain boundaries for all compositions probed via Raman and EDS (which did not

include SMW0). For concentrations lower than ~0.10%, W atoms are present exclusively inside SnO_2 grains and appear to replace Mn atoms there, thus increasing the amount of Mn_3O_4 precipitates. At higher concentrations, the excess W atoms precipitate as a $MnWO_4$ phase, formed at the expense of Mn_3O_4 precipitates. This process continues at higher WO_3 concentrations until the point of depletion of Mn_3O_4 precipitates, occurring at some WO_3 concentration in between 0.20% and 0.25%. The amount of $MnWO_4$, however, continues to increase, this time at the expense of Mn_3O_4 at grain boundaries. It is worth noting that, despite all microstructural changes, the addition of WO_3 did not change the mean grain size significantly.

Thermodynamic calculations from first principles (along with kinetic considerations) explained why phases Mn_3O_4 and $MnWO_4$ were present instead of starting MnO_2 and WO_3. Oxygen grand potential phase diagrams and a modified Ellingham diagram confirm that the starting phases are the most stables at room temperature, but predict three reactions at higher temperatures. First, MnO_2 is reduced to Mn_2O_3. Then, for the compositions considered here, in which the Mn:W ratio is greater than 1, part of Mn_2O_3 reacts with WO_3 to form $MnWO_4$. Last, Mn_2O_3 is reduced to form Mn_3O_4. During cooling, the phases Mn_3O_4 and $MnWO_4$ are then stabilized kinetically by the high cooling rate of the pellets.

These calculations also help to explain why the relative density of sintered pellets decreased significantly from composition 0.10% onwards: the reaction between WO_3 and the sintering agent (in its reduced form, Mn_2O_3) to form $MnWO_4$ becomes thermodynamically favorable below 600 °C. This reaction depletes part of the sintering agent long before sintering temperature is reached, compromising densification.

An analytical model of how the coefficients of the products in the synthesis reaction of the SMWx systems depend on x revealed a concave profile for the molar quantity of overall Mn_3O_4, with a maximum centered at x ~7.5. This profile was very similar to those presented by the nonlinear coefficient (α), the breakdown electric field (E_b) and the leakage current (I_l), indicating a correlation between the amount of overall Mn_3O_4 and varistor properties.

Tungsten addition to the SnO_2-MnO_2 system improved varistor properties up to 0.15 mol% of WO_3, promoting the increase of nonlinear coefficient to $\alpha \approx 6$ and breakdown electric field to E_b = 11.15 kV/cm, as well as reduction of leakage current. These results can be attributed to segregation of Mn caused by small additions of tungsten, helping the formation of defects that increase potential barrier at SnO_2/Mn_3O_4 interfaces. For SMW20, SMW25 and SMW30 systems, tungsten addition caused degradation of the potential barrier due to the formation of $MnWO_4$ phase by partial depletion of Mn_3O_4 phase, which decreased nonlinear coefficient and breakdown electric field to values as low as $\alpha \approx 2.5$ and E_b = 5.06 kV/cm.

This is the first report of varistor behavior in a SnO_2-based ternary system having a hexavalent donor as a dopant. Previous attempts using a different densifying agent, ZnO, resulted in typical linear behavior. Therefore, the sintering agent selected here (MnO_2) has proven crucial to nonlinearity. We expect this finding stimulates further investigations on SnO_2-based ternary systems containing hexavalent oxides, especially using other densifying agents, such as CoO.

Also, to the best of our knowledge, thermodynamic calculations from first principles and analytical modeling of synthesis equation coefficients have not been applied to varistor systems before, and Raman measurements are also not usual in this forum. Since these techniques played a fundamental role to characterize the phases observed here, and also to evidence the correlation

between the unreacted amount of densifying agent and the varistor properties, we believe the present paper will stimulate other research groups investigating varistors to employ them as additional tools.

Acknowledgments

The authors thank FINEP for financial support of CeMAT Laboratory facilities, where XRD and Raman measurements were performed. R. Mouta thanks A. S. de Menezes for enlightening discussions and all his support. C. C. Santos acknowledges funding from FAPEMA (Project Universal - 01290/16). This study was financed in part by the Coordenação de Aperfeiçoamento de Pessoal de Nível Superior - Brasil (CAPES) - Finance Code 001. The funding sources had no involvement in study design; in the collection, analysis or interpretation of data; in the writing of the report; or in the decision to submit the article for publication.

References

[1] P.R. Bueno, J.A. Varela, E. Longo, SnO_2, ZnO and related polycrystalline compound semiconductors: An overview and review on the voltage-dependent resistance (non-ohmic) feature, J. Eur. Ceram. Soc. 28 (2008) 505–529. doi:10.1016/j.jeurceramsoc.2007.06.011.

[2] D.R. Clarke, Varistor Ceramics, J. Am. Ceram. Soc. 82 (2004) 485–502. doi:10.1111/j.1151-2916.1999.tb01793.x.

[3] Y. Gong, R. Chu, Z. Xu, J. Sun, F. Chao, S. Ma, J. Hao, H. Li, G. Li, Electrical properties of Ta_2O_5-doped TiO_2 varistor ceramics sintered at low-temperature, Ceram. Int. 41 (2015) 9183–9187. doi:10.1016/j.ceramint.2015.03.082.

[4] T.R.N. Kutty, S. Philip, Low voltage varistors based on $SrTiO_3$ ceramics, Mater. Sci. Eng. B. 33 (1995) 58–66. doi:10.1016/0921-5107(94)01205-9.

[5] T.G. Wang, G.Q. Shao, W.J. Zhang, X.B. Li, X.H. Yu, Electrical properties of Pr_6O_{11}-doped WO_3 capacitor–varistor ceramics, Ceram. Int. 36 (2010) 1063–1067. doi:10.1016/j.ceramint.2009.12.004.

[6] J.A. Aguilar-Martínez, P. Zambrano-Robledo, S. García-Villarreal, M.B. Hernández, E. Rodríguez, L. Falcon-Franco, Effect of high content of Co_3O_4 on the structure, morphology, and electrical properties of (Cr,Sb)-doped SnO_2 varistors, Ceram. Int. 42 (2016) 7576–7582. doi:10.1016/j.ceramint.2016.01.165.

[7] S.A. Pianaro, P.R. Bueno, E. Longo, J.A. Varela, A new SnO_2-based varistor system, J. Mater. Sci. Lett. 14 (1995). doi:10.1007/BF00253373.

[8] M.O. Orlandi, P.R. Bueno, E.R. Leite, E. Longo, Nonohmic behavior of $SnO_2.MnO_2$-based ceramics, Mater. Res. 6 (2003) 279–283. doi:10.1590/S1516-14392003000200025.

[9] S.A. Pianaro, P.R. Bueno, E. Longo, J.A. Varela, Microstructure and electric properties of a SnO_2 based varistor, Ceram. Int. 25 (1999) 1–6. doi:10.1016/S0272-8842(97)00076-X.

[10] L. Perazolli, A.Z. Simões, U. Coleto, F. Moura Filho, S. Gutierrez, C.O.P. Santos, J.A.G. Carrió, R.F.C. Marques, J.A. Varela, Structural and microstructural behaviour of SnO_2

dense ceramics doped with ZnO and WO_3, Mater. Lett. 59 (2005) 1859–1865. doi:10.1016/j.matlet.2005.02.022.

[11] M.A.L. Margionte, A.Z. Simões, C.S. Riccardi, A. Ries, F.M. Filho, L. Perazolli, J.A. Varela, Nonlinear characteristics of Cr_2O_3, WO_3, ZnO and CoO doped SnO_2 varistors, Mater. Lett. 60 (2006) 142–146. doi:10.1016/j.matlet.2005.08.006.

[12] S.P. Ong, L. Wang, B. Kang, G. Ceder, Li−Fe−P−O_2 Phase Diagram from First Principles Calculations, Chem. Mater. 20 (2008) 1798–1807. doi:10.1021/cm702327g.

[13] J. Wu, S.S. Pramana, S.J. Skinner, J.A. Kilner, A.P. Horsfield, Why Ni is absent from the surface of $La_2NiO_{4+\delta}$?, J. Mater. Chem. A. 3 (2015) 23760–23767. doi:10.1039/C5TA03759J.

[14] L. Shi, A. Xu, T.S. Zhao, Formation of Li_3O_4 nano particles in the discharge products of non-aqueous lithium–oxygen batteries leads to lower charge overvoltage, Phys. Chem. Chem. Phys. 17 (2015) 29859–29866. doi:10.1039/C5CP03886C.

[15] S.P. Ong, A. Jain, G. Hautier, B. Kang, G. Ceder, Thermal stabilities of delithiated olivine MPO_4 (M=Fe, Mn) cathodes investigated using first principles calculations, Electrochem. Commun. 12 (2010) 427–430. doi:10.1016/j.elecom.2010.01.010.

[16] C.B. Barber, D.P. Dobkin, H. Huhdanpaa, The quickhull algorithm for convex hulls, ACM Trans. Math. Softw. 22 (1996) 469–483. doi:10.1145/235815.235821.

[17] M.-H. Chen, A. Emly, A. Van der Ven, Anharmonicity and phase stability of antiperovskite Li_3OCl, Phys. Rev. B. 91 (2015) 214306. doi:10.1103/PhysRevB.91.214306.

[18] A. Jain, G. Hautier, S.P. Ong, C.J. Moore, C.C. Fischer, K.A. Persson, G. Ceder, Formation enthalpies by mixing GGA and GGA+U calculations, Phys. Rev. B. 84 (2011) 045115. doi:10.1103/PhysRevB.84.045115.

[19] A. Jain, S.P. Ong, G. Hautier, W. Chen, W.D. Richards, S. Dacek, S. Cholia, D. Gunter, D. Skinner, G. Ceder, K.A. Persson, Commentary: The Materials Project: A materials genome approach to accelerating materials innovation, APL Mater. 1 (2013) 011002. doi:10.1063/1.4812323.

[20] S.P. Ong, S. Cholia, A. Jain, M. Brafman, D. Gunter, G. Ceder, K.A. Persson, The Materials Application Programming Interface (API): A simple, flexible and efficient API for materials data based on REpresentational State Transfer (REST) principles, Comput. Mater. Sci. 97 (2015) 209–215. doi:10.1016/j.commatsci.2014.10.037.

[21] S.P. Ong, W.D. Richards, A. Jain, G. Hautier, M. Kocher, S. Cholia, D. Gunter, V.L. Chevrier, K.A. Persson, G. Ceder, Python Materials Genomics (pymatgen): A robust, open-source python library for materials analysis, Comput. Mater. Sci. 68 (2013) 314–319. doi:10.1016/j.commatsci.2012.10.028.

[22] L. Wang, T. Maxisch, G. Ceder, A First-Principles Approach to Studying the Thermal Stability of Oxide Cathode Materials, Chem. Mater. 19 (2007) 543–552. doi:10.1021/cm0620943.

[23] K. Persson, Materials Data on O_2 (SG:12) by Materials Project, (2014). doi:10.17188/1189289.

[24] M.W. Chase Jr, NIST-JANAF thermochemical tables, J. Phys. Chem. Ref. Data, Monogr. 9 (1998).

[25] D. Burgess, Thermochemical Data, in: P. Linstrom, W. Mallard (Eds.), NIST Chem. WebBook, NIST Stand. Ref. Database Number 69, National Institute of Standards and Technology, Gaithersburg, MD, n.d. doi:10.18434/T4D303.

[26] M.A.L. Margionte, A.Z. Simões, C.S. Riccardi, F.M. Filho, A. Ries, L. Perazolli, J.A. Varela, WO_3 and ZnO-doped SnO_2 ceramics as insulating material, Ceram. Int. 32 (2006) 713–718. doi:10.1016/j.ceramint.2005.05.008.

[27] D. Gouvea, A. Smith, J.-P. Bonnet, Manganese segregation on the surface of SnO_2 based powders, Eur. J. Solid State Inorg. Chem. 33 (1996) 1015–1023. http://cat.inist.fr/?aModele=afficheN&cpsidt=2545824.

[28] D. Gouvea, A. Smith, J.. Bonnet, J.. Varela, Densification and coarsening of SnO_2-based materials containing manganese oxide, J. Eur. Ceram. Soc. 18 (1998) 345–351. doi:10.1016/S0955-2219(97)00127-1.

[29] B. Lafuente, R.T. Downs, H. Yang, N. Stone, 1. The power of databases: The RRUFF project, in: Highlights Mineral. Crystallogr., DE GRUYTER, Berlin, München, Boston, n.d.: pp. 1–30. doi:10.1515/9783110417104-003.

[30] M.-C. Bernard, Electrochromic Reactions in Manganese Oxides, J. Electrochem. Soc. 140 (1993) 3065. doi:10.1149/1.2220986.

[31] F. Buciuman, F. Patcas, R. Craciun, D.R.T. Zahn, Vibrational spectroscopy of bulk and supported manganese oxides, Phys. Chem. Chem. Phys. 1 (1999) 185–190. doi:10.1039/a807821a.

[32] Y.-F. Han, F. Chen, Z. Zhong, K. Ramesh, L. Chen, E. Widjaja, Controlled Synthesis, Characterization, and Catalytic Properties of Mn_2O_3 and Mn_3O_4 Nanoparticles Supported on Mesoporous Silica SBA-15, J. Phys. Chem. B. 110 (2006) 24450–24456. doi:10.1021/jp064941v.

[33] M.N. Iliev, M.M. Gospodinov, A.P. Litvinchuk, Raman spectroscopy of $MnWO_4$, Phys. Rev. B. 80 (2009) 212302. doi:10.1103/PhysRevB.80.212302.

[34] P. Patureau, M. Josse, R. Dessapt, J.-Y. Mevellec, F. Porcher, M. Maglione, P. Deniard, C. Payen, Incorporation of Jahn–Teller Cu^{2+} Ions into Magnetoelectric Multiferroic $MnWO_4$: Structural, Magnetic, and Dielectric Permittivity Properties of $Mn_{1-x}Cu_xWO_4$ ($x \leq 0.25$), Inorg. Chem. 54 (2015) 10623–10631. doi:10.1021/acs.inorgchem.5b01416.

[35] C. Klingsberg, R. Roy, Solid-Solid and Solid-Vapor Reactions and a New Phase in the System Mn-O, J. Am. Ceram. Soc. 43 (1960) 620–626. doi:10.1111/j.1151-2916.1960.tb13630.x.

[36] K.T. Jacob, A. Kumar, G. Rajitha, Y. Waseda, Thermodynamic Data for Mn_3O_4, Mn_2O_3 and MnO_2, High Temp. Mater. Process. 30 (2011). doi:10.1515/htmp.2011.069.

[37] M.R. Cássia-Santos, V.C. Sousa, M.M. Oliveira, F.R. Sensato, W.K. Bacelar, J.W. Gomes, E. Longo, E.R. Leite, J.A. Varela, Recent research developments in SnO_2-based varistors, Mater. Chem. Phys. 90 (2005) 1–9. doi:10.1016/j.matchemphys.2003.12.014.

[38] M.M. Oliveira, P.R. Bueno, E. Longo, J.A. Varela, Influence of La_2O_3, Pr_2O_3 and CeO_2 on the nonlinear properties of SnO_2 multicomponent varistors, Mater. Chem. Phys. 74 (2002) 150–153. doi:10.1016/S0254-0584(01)00458-8.

[39] M.M. Oliveira, J.H.G. Rangel, V.C. de Sousa, E. Longo, R.N. R. Filho, Revisão: efeito dos metais doadores nas propriedades elétricas e microestruturais dos varistores cerâmicos à base de SnO_2, CerâMica. 54 (2008) 296–302. doi:10.1590/S0366-69132008000300005.